

**Final report for MSc Project**

---

**Investigation of Residual Stress in Nitinol through FIB-DIC**

---

**Jacob Schneider-Martin**

Supervisor(s): Professor David Nowell

Submitted in partial fulfilment of the requirements for the award of MSc in Biomedical  
Engineering from Imperial College London

September 2019

Word count: 5929

## **Abstract**

Superelastic nitinol, which is an alloy widely used in minimally-invasive medical devices, can crimp to a low profile, be loaded into a delivery catheter, and then self-expand at body temperature. During an implant procedure, residual stress can be induced, which can affect the fatigue performance of the nitinol device. Residual stress in nitinol is currently predicted using finite element (FE) models, which are not validated and use macro-scale properties of nitinol to predict micron-scale residual stress. The FIB-DIC technique, which combines focused ion beam (FIB) milling on a scanning electron microscope (SEM) with digital image correlation (DIC), has shown to be an effective tool to measure residual stress in materials. In this research, FIB-DIC was used for the first time to measure residual stress in superelastic nitinol. The FIB-DIC method was validated by measuring the residual stress in a plastically bent MP35N beam and comparing the experimental results to analytical solutions. The overall FIB-DIC results followed the residual stress trend predicted by the analytical solutions, and differences between the experimental and analytical results were ascribed to the electron beam source of the SEM nearing the end of its lifecycle. The FIB-DIC measurement of residual stress in nitinol was in close agreement with the yield stress of nitinol, which was expected. FIB-DIC may be used as a powerful tool to build understanding of the mechanics of superelastic nitinol and has the potential to help improve the performance of state-of-the-art superelastic material models for the medical device industry.

## **Acknowledgements**

I would like to thank Professor David Nowell for his help, advice, and support during this project. I would also like to thank Medtronic for financial support. I am appreciative of the technical assistance from Enrico Salvati from the University of Oxford and Curtis Goreham-Voss, Michael Schendel, Stu Kari, Tony Anderson, and Shivram Sridhar from Medtronic. Finally, I am grateful to the Medtronic Structural Integrity group for allowing me to pursue my master's degree.

## TABLE OF CONTENTS

Abstract .....	2
Acknowledgements .....	2
1. Introduction.....	4
1.1. Residual Stress Background.....	4
1.2. Focused Ion Beam-Digital Image Correlation Background.....	4
1.3. Investigation of Residual Stress in Nitinol.....	8
2. FIB-DIC Method.....	9
2.1. Speckle Pattern Application .....	9
2.2. SEM Imaging Conditions.....	11
2.3. FIB Milling Conditions and Geometry .....	15
2.4. DIC Analysis .....	17
2.5. Calculation of Residual Stress.....	18
3. FIB-DIC Validation.....	19
3.1. Validation Method.....	19
3.2. Validation Results.....	22
3.2.1. Strain Relief Measurements.....	22
3.2.2. Residual Stress Results.....	25
4. Nitinol Test.....	26
4.1. Test Method.....	26
4.2. Test Results .....	27
5. Discussion & Conclusion.....	28
5.1. FIB-DIC Validation .....	28
5.2. Nitinol Test .....	28
6. References.....	30

## 1. Introduction

### 1.1. Residual Stress Background

Residual stress can be critical to the structural integrity of devices. When a load that induces plasticity in a material is removed, elastic springback occurs, which produces both tensile and compressive residual stress, which are locked in to the material [1]. While tensile residual stress can be detrimental to device performance, compressive residual stress can be beneficial and is often deliberately induced in manufacturing, using processes such as surface rolling and shot peening [2]. Nearly all manufacturing processes, though, create some amount of residual stress.

Residual stress can occur over a variety of length scales [3]:

- Type I: global stress that varies over distances larger than a grain and resembles the macroscopic stress value
- Type II: intergranular, micron-scale stress that varies over distances similar to a grain
- Type III: intragranular, nano-scale stress that varies within a grain
- Total residual stress in a material is the sum of Type I, II, and III stresses

Measuring Type II and III residual stress is important, as micron and nano-scale residual stress can cause crack initiation at the macro-scale. There are several experimental techniques used to measure residual stress, but these techniques have limitations. The macro-scale hole drilling technique, for example, incrementally removes material from a test specimen, releasing residual stress and allowing the material to relax to a new equilibrium state. The relaxation strain is captured using strain gauges; this allows the residual stress originally present in the material to be calculated using Hooke's Law [4]. This technique, though, is only able to resolve residual stress in materials that are both large enough to have strain gauges mounted and deep enough to have a hole drilled. X-ray diffraction (XRD), a micro-scale technique, detects Type II and III residual stress by measuring the diffraction of an x-ray through a material, which changes based on the lattice spacing of the material, which is dependent on the elastic strain present. However, XRD can only measure residual stresses that are present in a very shallow layer of the material, and the technique does not work with all materials [5, 6].

### 1.2. Focused Ion Beam-Digital Image Correlation Background

FIB-DIC, which combines focused ion beam (FIB) milling on a scanning electron microscope (SEM) with digital image correlation (DIC), has emerged as a powerful tool to measure micron-scale residual stress. In FIB-DIC, which is effectively a down-scaling of the macro-scale hole drilling method, a FIB removes material from the surface of a plastically deformed test specimen, which releases residual stress. As the stress is released, the specimen undergoes relaxation and moves to a new equilibrium state, and the SEM captures a series of images. These images are then analysed using DIC, which tracks the displacement of the specimen during relaxation and calculates the strain across the surface of the sample. The residual stress originally present in the material can then be calculated using a plane stress approximation [7]. A diagram of a typical FIB/SEM system is shown below in Figure 1.

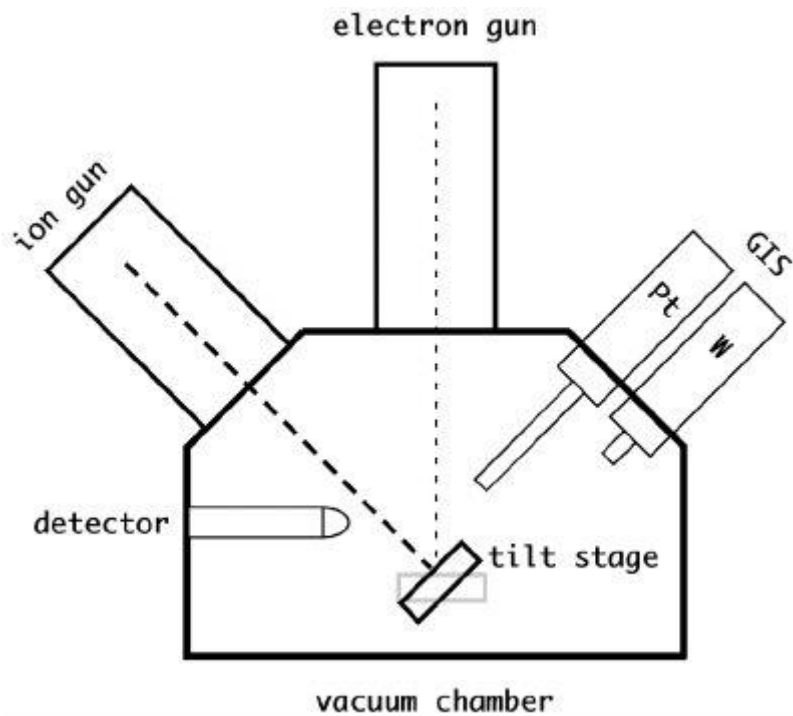
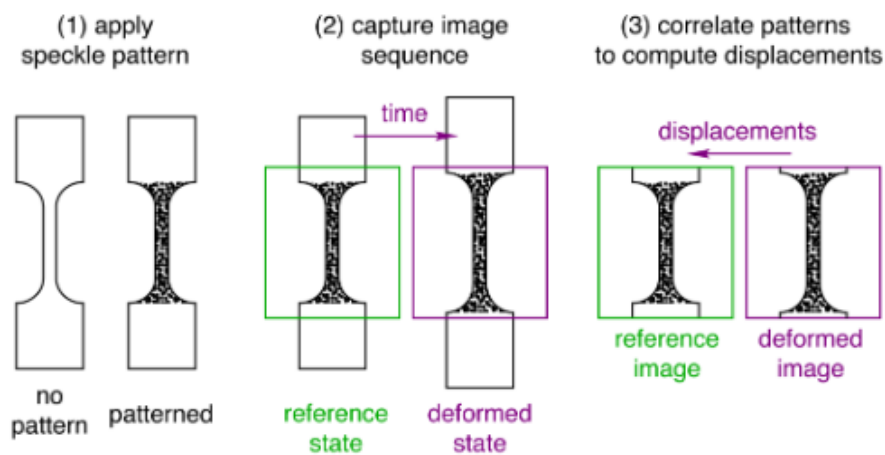


Figure 1: Diagram of a focused ion beam-scanning electron microscope (FIB/SEM) system [8].

DIC is a non-contact surface displacement measurement technique that can measure the deformation of solid objects. A tracking pattern, known as a speckle pattern, is first applied to a specimen. As the specimen is deformed in a test, the speckle pattern deforms with it, and DIC tracks this pattern across a sequence of images, as shown in Figure 2. DIC first divides the initial image taken, known as the reference image, into small, recognizable portions, called subsets. DIC then tracks the movement of the test specimen by matching the deformed subsets back to the reference subsets. Once the subsets are matched, the DIC software calculates the relative displacement and deformation of each subset, which allows the strain across the entire surface of the test specimen to be calculated [9]. Sub-pixel displacement resolution can be obtained using DIC.



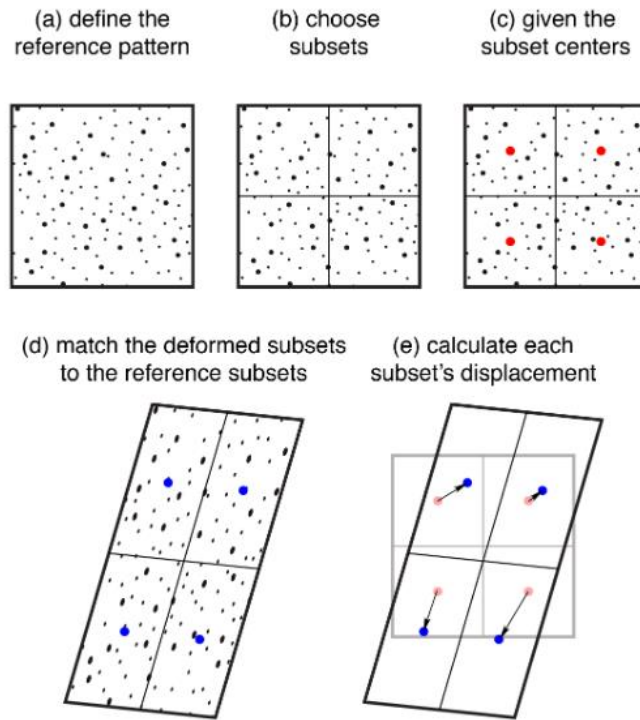


Figure 2: Top: Specimen deformation and DIC displacement calculation. Bottom: DIC subset correlation and displacement calculation [9].

The quality of the DIC results is highly dependent on the quality of the speckle pattern. The speckle pattern should be random, isotropic, high contrast, and have an even distribution between black and white speckles, as seen in Figure 3 [9]. The pattern must also be able to move and deform with the sample during the test.

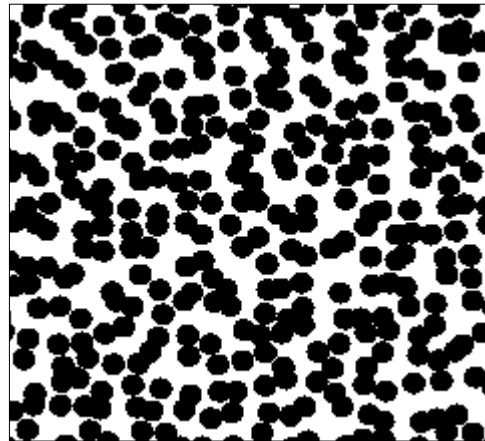


Figure 3: Ideal speckle pattern generated from Speckle Generator™ application [10].

DIC was first used by Sutton in 1988, but its use has been growing recently in a variety of applications, from material characterisation and finite element (FE) model validation to analysis of magnetic resonance and computed tomography images [11-13]. DIC is most often used to analyse images captured from optical microscopes. The Medtronic Structural Integrity group in Mounds View, Minnesota has a Vic-3D Micro™ system from Correlated Solutions, Inc. This is a stereo microscope system with high resolution that is currently being used to examine the validity of FE models of different Medtronic Structural Heart products, as seen in Figure 4.

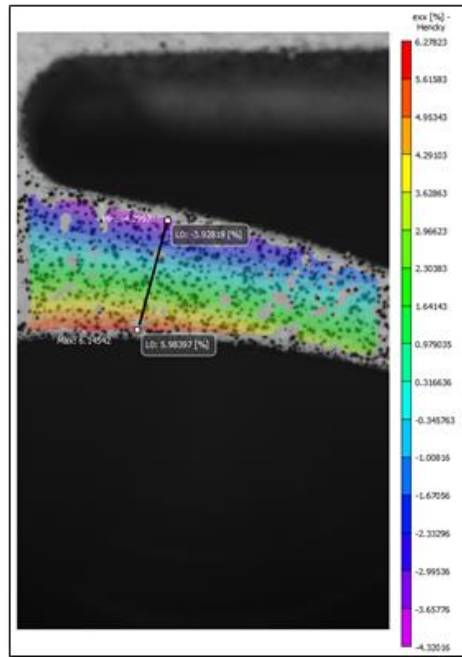


Figure 4: Screenshot from Medtronic optical DIC analysis showing the distribution of strain along the x-axis across a specimen in a test.

FIB-DIC was first used by Kang and Sabaté in the mid-2000s and since then has been used to probe residual stress in a wide variety of materials [14, 15]. FIB-DIC has been growing in use, and several FIB milling geometries have been developed, as seen in Figure 5 [6].

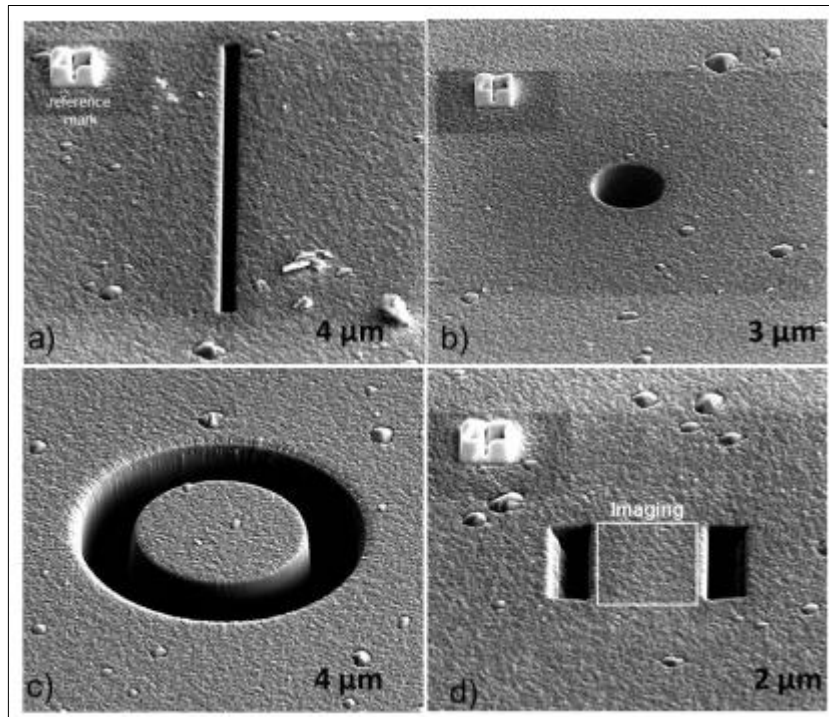


Figure 5: Different FIB milling geometries used in FIB-DIC experiments [6].

Investigations have validated different geometries by comparing the residual stress results from FIB-DIC to the results from theoretical solutions, FE simulations, XRD, and wafer curvature measurements [7, 16-19]. The iSTRESS project, a collaboration between multiple universities, industrial partners, and the National Physical Laboratory (NPL), has begun to develop a pre-standardisation of the FIB-DIC technique, and an extensive “Good Practice Guide for Measuring Residual Stresses using FIB-DIC” was published in 2018 from NPL [20, 6].

Experiments using FIB-DIC have investigated topics such as residual stress induced from shot peening to residual stress in thin films [21, 22]. Research from Imperial College London has used DIC to extensively study the deformation, modeling, and propagation of fatigue cracks at the micro-scale [23-26]. Researchers from Imperial, in collaboration with industrial partners, have also used DIC to examine the impact of residual stress on the fatigue life of materials [27].

### 1.3. Investigation of Residual Stress in Nitinol

Nitinol is a widely used nickel-titanium alloy in minimally-invasive medical devices, and its superelastic shape-memory properties allow it to crimp to a low profile and self-expand at body temperature, as shown in Figure 6. After a nitinol device is crimped down and expanded, though, the device has a permanent set: there is a slight outer diameter loss, and the device is unable to fully return to its original relaxed size. This is due to significant residual stress. The Medtronic Structural Integrity group has shown through testing that there is a strong correlation between residual stress and fatigue performance for nitinol devices.

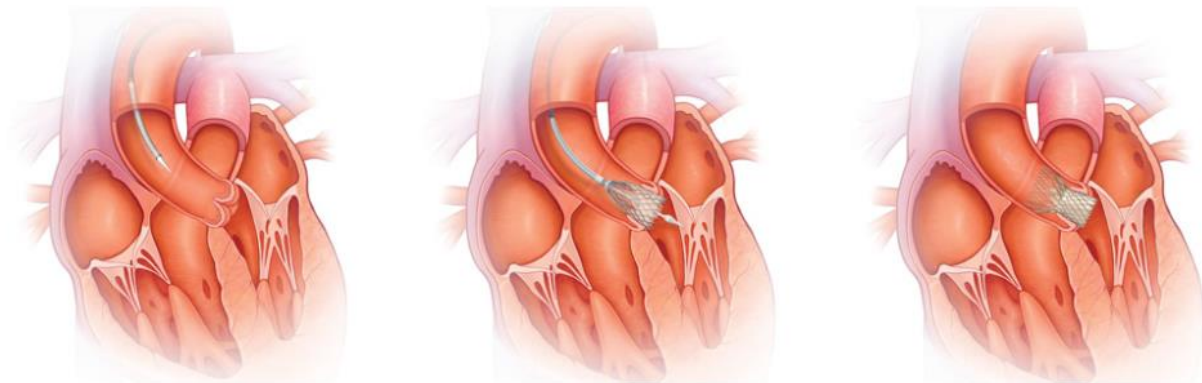


Figure 6: Illustration of deployment procedure for a nitinol transcatheter aortic valve replacement [28].

Residual stress in nitinol devices are currently predicted via FE simulations, but these models are not validated and use macro-scale properties of nitinol to make predictions about micron-scale residual stress. Experimentally measuring residual stress could help build understanding of the complex mechanics of nitinol and improve the performance of nitinol material models. Although previous research has investigated nitinol’s properties using DIC on an SEM, there have not been investigations into residual stress in nitinol using FIB-DIC. The aim of this research was to validate the FIB-DIC method and measure micron-scale residual stress in nitinol using FIB-DIC.



## 2. FIB-DIC Method

There are five primary steps to the FIB-DIC method:

1. Speckle Pattern Application
2. Selection of SEM Imaging Conditions
3. Selection of FIB Milling Conditions
4. DIC Analysis
5. Calculation of Residual Stress

These steps were consistent for both the validation experiment and nitinol test.

### 2.1. Speckle Pattern Application

Although there are many methods to apply a speckle pattern, this investigation followed the general strategy outlined by Everaerts, in which a sample is first electropolished and then sputter coated [29]. This procedure has several benefits: Electropolishing removes much of the residual stress that may be present near the surface of the material due to manufacturing, which in most cases is not the residual stress of interest to investigators. Additionally, electropolishing removes the natural surface texture present on materials and allows for an improved, artificial speckle pattern to be applied through sputter coating, which is fast and cost-effective.

Samples were first electropolished at an internal Medtronic prototyping site and then sputter coated with a thin layer of Au-Pd using a Denton Desk I sputter coater at Medtronic Operational Headquarters in Fridley, Minnesota. An image of a sample after electropolishing and Au-Pd sputtering is shown in Figure 7.

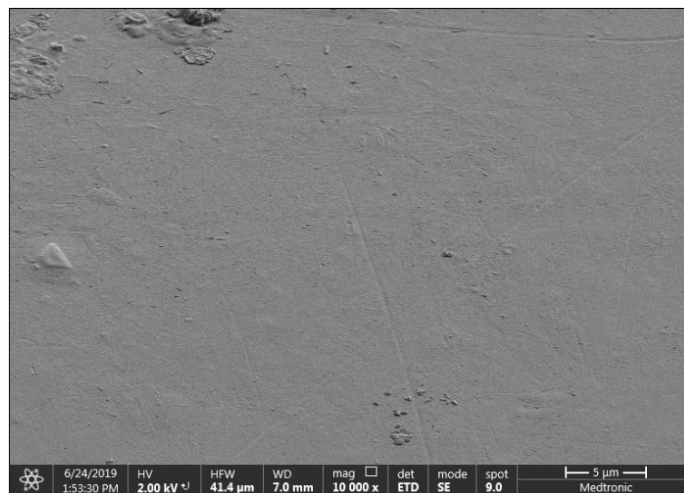


Figure 7: Specimen after electropolishing and Au-Pd sputtering.

The sputter coated layer needed to be as thin as possible so that the deposition layer would not migrate from the surface of the test specimen during the FIB-DIC procedure, which could artificially alter the DIC results. However, if the Au-Pd deposition layer was too thin or not uniform, the speckle pattern would not function as intended. Since the Denton Desk I sputter coater does not have deposition layer thickness control, only the amount of time a specimen was sputtered could be controlled. Five samples were placed in the sputter coater for times ranging from 30 to 240 seconds.

To measure the thickness of the deposition layer in the different samples, the samples were placed in the FEI Scios™ DualBeam™ FIB/SEM system from Thermo Fisher Scientific, Inc. at Medtronic Operational Headquarters, and the FIB milled out a section of the sample, as shown in Figure 8. This allowed the cross

section of the deposition layer to be viewed. To improve the ability to resolve the top of the deposition layer, a thin layer of Pt was deposited by the FIB on top of the Au-Pd. The thickness of the deposition layer was then measured.

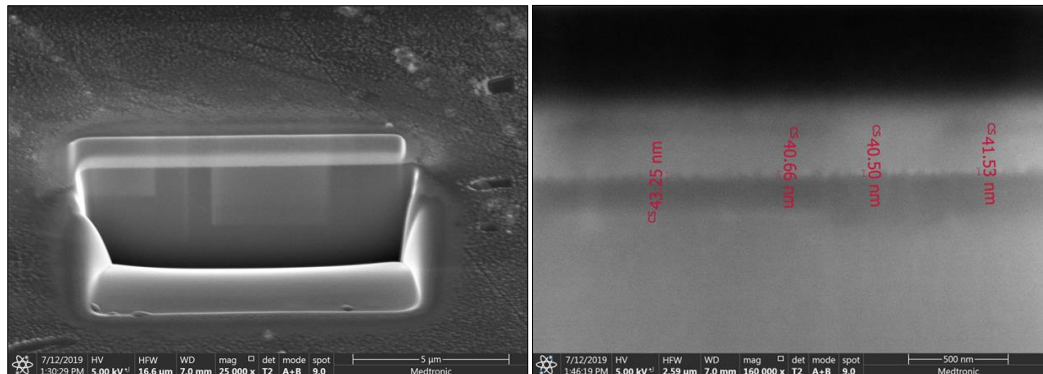


Figure 8: Left: Zoomed-out view of cross sectioned sputter coated sample. Right: Zoomed-in view of Au-Pd deposition layer covered with Pt and thickness measurements.

It was found that 45 seconds in the sputter coater was the minimum amount of time needed for a uniform deposition layer. This amount of time yielded an Au-Pd deposition layer with a thickness of around 41 nm, as shown above in Figure 8.

After the sample was sputter coated, a bitmap image of a speckle pattern was created using the Speckle Generator™ application from Correlated Solutions and loaded onto the FIB [10]. This application allows the size, randomness, and density of the speckles to be changed, and a screenshot of the application is shown in Figure 9.

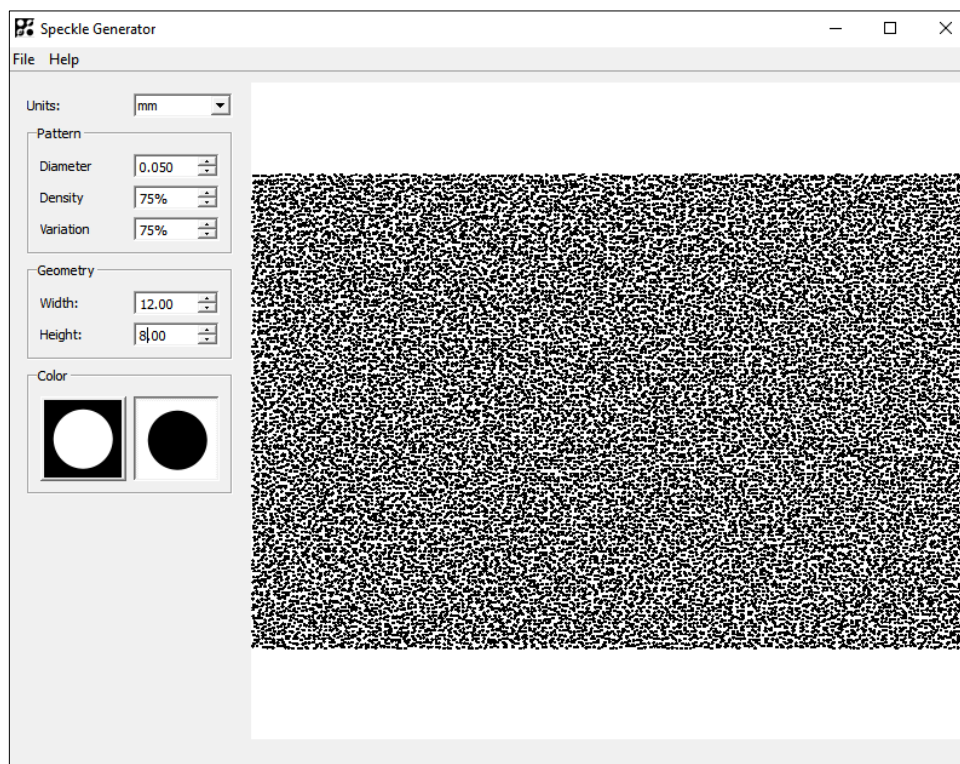


Figure 9: Screenshot of Speckle Generator™ application [10].

For the DIC software to work optimally, speckles should be 5 pixels in length, with at least a 5 pixel spacing between them. Once the resolution and horizontal field width (HFW) of an upcoming FIB-DIC experiment are known, the length of each pixel can be calculated. The optimal speckle size can then be determined and input into the diameter control in the Speckle Generator™ application.

Once the bitmap speckle image was loaded onto the FIB, the FIB milled .5 nm into the white area of the speckle pattern. This created a high contrast, random speckle pattern with an even distribution between white and black speckles that were of the optimal size, as shown in Figure 10. The process of milling out a shallow section of material using a bitmap speckle pattern has also been implemented by past researchers to create effective tracking patterns, but the speckle patterns in this investigation are of an improved quality due to a higher degree of randomness [21].

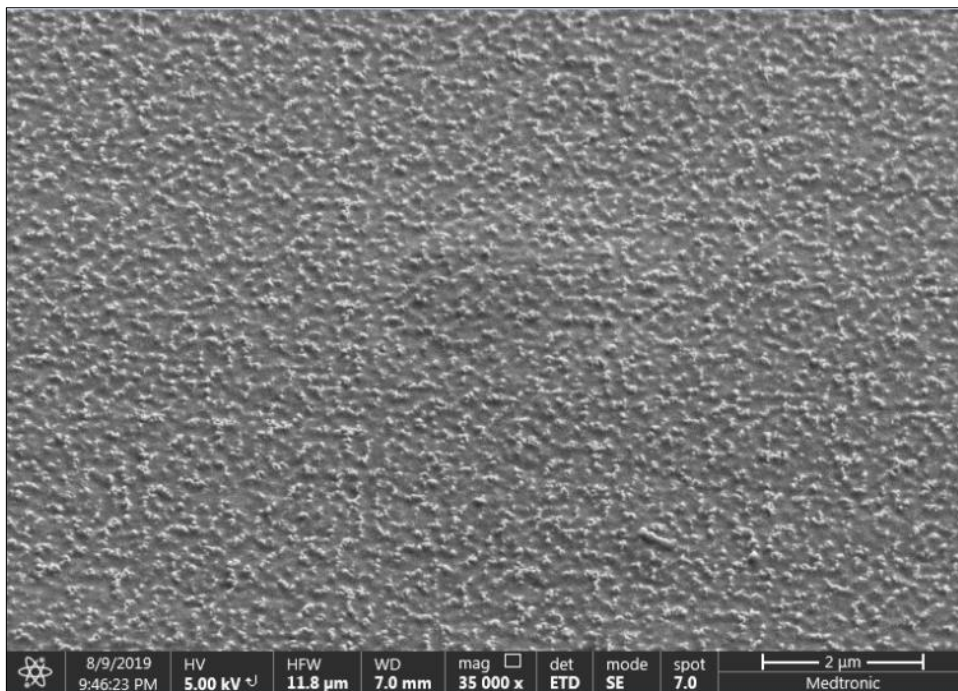


Figure 10: Speckle pattern on a sample after electropolishing, Au-Pd sputtering, and milling out the bitmap pattern.

## 2.2. SEM Imaging Conditions

DIC conducted using SEM images involves challenges that are not present in optical DIC. This is due to differences in how the images are acquired. In an SEM, images are captured using a raster scan, as shown in Figure 11, which can cause distortions in DIC [6].

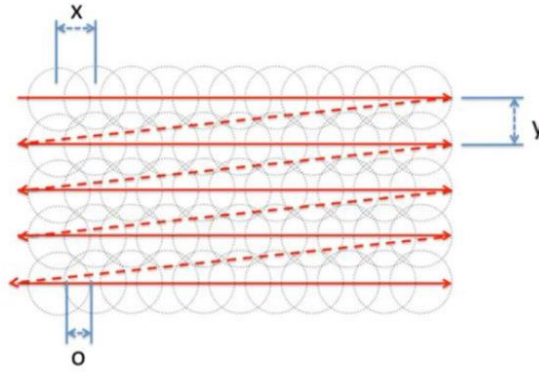


Figure 11: Raster scan pattern used for image capture on an SEM [6].

At low SEM magnifications, there may be distortions at the edge of the image: the magnetic lenses of the SEM induce large changes in the magnetic field at the edges of the image, where the electron beam must travel furthest, and there are imperfections in all magnetic lenses, which causes these distortions. For most DIC experiments performed on an SEM, this distortion does not affect the results, as this artefact is only present at low SEM magnifications.

At high SEM magnifications, artefacts may arise due to imperfections in the SEM's digital-to-analogue converter (DAC). As the electron beam moves through the raster scan, the DAC could appear linear, but may have a ramp that can vary throughout the experiment; this can generate small errors in the pixel positions of the scan. This distortion manifests as vertical and horizontal bands in DIC, which are shown in Figure 12 [6].

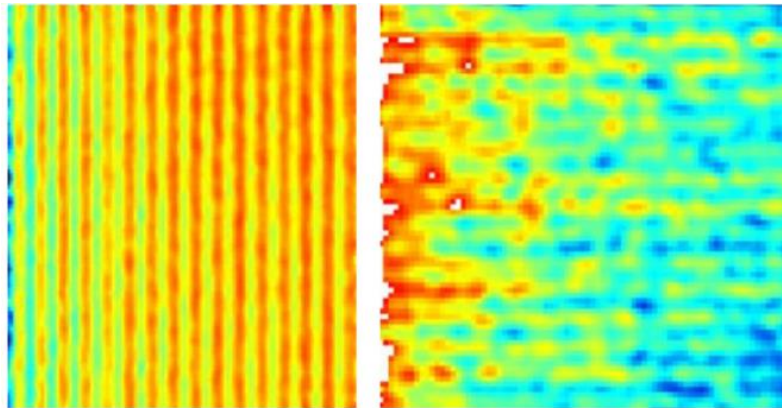


Figure 12: Vertical and horizontal band distortions in high magnification SEM imaging [6].

Although these distortions are the most common distortion found in FIB-DIC experiments, they are small in magnitude compared to the strain relief observed in most experiments and should not have a significant impact on results. Additionally, larger subset sizes can reduce the effect of this artefact, as shown in Figure 13 [6].



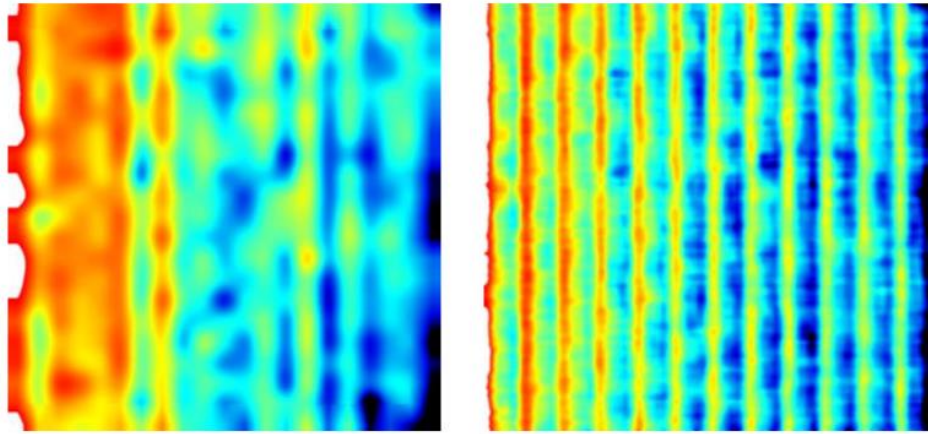


Figure 13: Left: DIC image with larger subset size and reduced distortions. Right: Same DIC image with smaller subset size [6].

Integrating the SEM images can also reduce artefacts and increase the signal to noise ratio of the scan. Using a high frame rate to capture the images and integrating over several frames reduces the amount of noise present in the SEM. Image integration and the subsequent reduction of noise can be seen in Figure 14 [6].

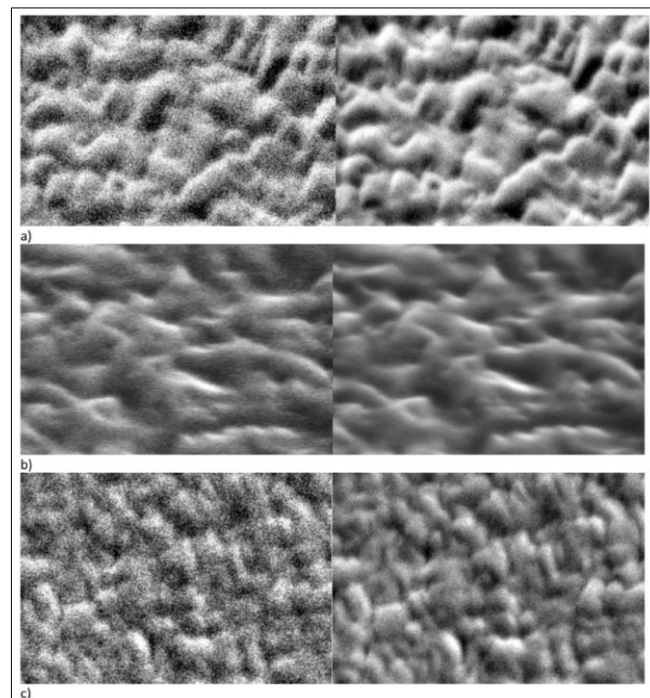


Figure 14: In three different SEM systems, Left: Single, noisy images. Right: Integrated images, with reduced noise [6].

There are numerous SEM scanning parameters, and past studies have analysed the effect that different parameters have on SEM distortions [13, 19, 30]. Every SEM is different, though, so to characterise the instabilities present on the FEI FIB/SEM system, an experiment was conducted following Mansilla's

procedure [30]. In this experiment, an SEM image of a specimen was acquired, the stage was moved and then returned to its original position after three minutes, and then a second SEM image was acquired. Six image pairs were captured using different SEM scanning parameters, as shown in Table 1. For each image pair, one SEM parameter was changed.

Table 1: Image Pairs and SEM Parameters

Image Pair Number	Integration	Drift Correction	Dwell Time	Resolution
1	16	Yes	1	768x512
2	16	Yes	3	768x512
3	16	No	3	768x512
4	4	Yes	3	768x512
5	4	Yes	10	768x512
6	4	Yes	10	1536x1024

Each image pair was then correlated using DIC, and the SEM instabilities were analysed by calculating the standard deviation of the displacement of the image in the horizontal and vertical directions. This was found by measuring each pixel's displacement in the x and y directions and using Formula 1:

$$SD_x^{DIC} = \sqrt{\frac{1}{N} \sum_i (\Delta_x^i)^2} \quad SD_y^{DIC} = \sqrt{\frac{1}{N} \sum_i (\Delta_y^i)^2} \quad (1)$$

With i being the pixel number and N being the total number of pixels in the image [30]. Using each pixel's displacement, rather than the image drift as a whole, generates a more accurate characterisation of SEM instability. The results from the instability characterisation are shown below in Table 2 and display the standard deviation of the displacements in the horizontal and vertical directions and the relative standard deviation, which is normalised for SEM image size and is a better comparator of instability between different SEM systems.

Table 2: SEM Instability Results

Image Pair Number	$SD_x^{DIC}$ (nm)	$SD_y^{DIC}$ (nm)	Relative $SD_x^{DIC}$ ( $\times 10^{-5}$ )	Relative $SD_y^{DIC}$ ( $\times 10^{-5}$ )
1	1.6	1.4	13.5	18.8
2	.34	.32	2.88	4.04
3	.43	.33	3.61	4.22
4	.76	.68	6.48	8.63
5	.43	.36	3.62	4.59
6	.65	.69	5.47	8.85
Acceptance Criterion			< 5	< 5

As seen from Table 2, image pairs 2, 3, and 5 were all below the acceptance criterion developed by Mansilla and are therefore deemed acceptable SEM parameters. Pair 2 had the lowest distortions, and the SEM parameters used in pair 2 were used in all SEM experiments in this investigation. An image of the DIC analysis of image pair 2 is shown in Figure 15.

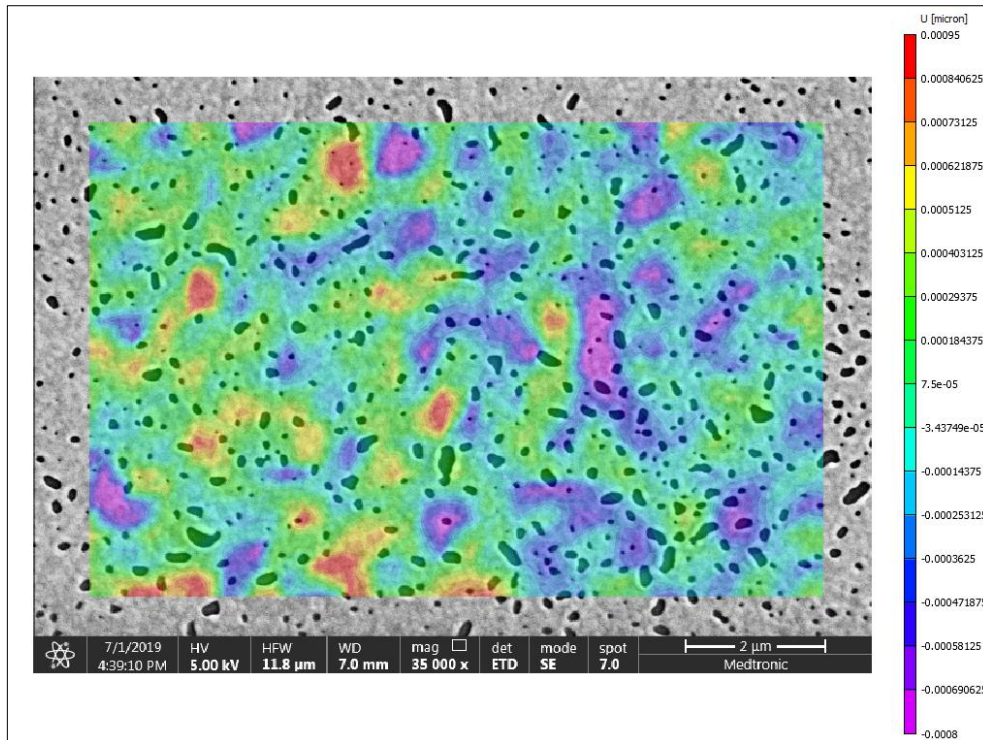


Figure 15: SEM instability results in the x direction using parameters from image pair 2.

In the above image, the maximum U displacement – the displacement along the x-axis – is .00095 microns. Each pixel in this image is .015 microns in length, so this displacement distortion is roughly 6% of one pixel. This gives a more intuitive measure of just how small the DIC distortions are when using the SEM parameters from image pair 2. Additionally, a visual inspection shows that the distortions are random throughout the image and do not have a directional bias. Finally, during the actual FIB-DIC experiments, multiple images were captured at each imaging step to reduce the effects of small scanning errors.

### 2.3. FIB Milling Conditions and Geometry

There are also a number of FIB parameters that need to be controlled. It is important to know how deep the FIB is milling into the material, which depends on the FIB dose and material-specific sputtering rate. Depth profiling was completed for both MP35N and nitinol by milling out small sections of the sample and measuring the depth. This process was repeated with different FIB doses to construct a milling calibration curve, as seen in Figure 16:

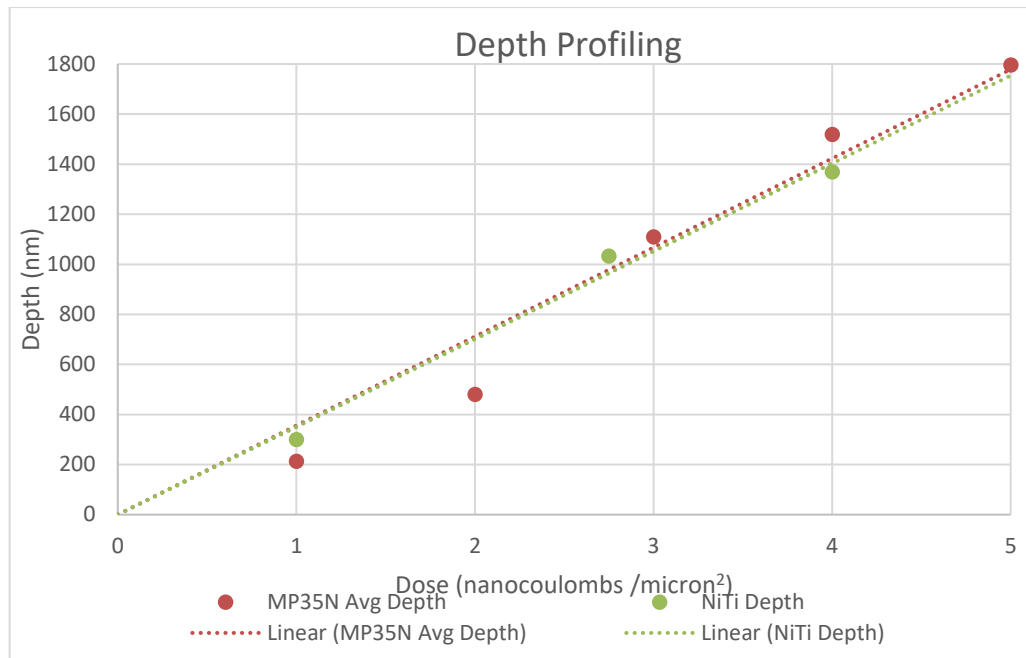


Figure 16: Depth Profiling for MP35N and nitinol.

As seen from the calibration curve, MP35N and nitinol have very similar milling rates. When performing milling in a FIB-DIC test, it is critical to not use a high FIB dose, as the FIB can damage the material and induce residual stress. In this investigation, incremental milling was performed, which removed 250 nm in depth from the material during each milling step, which minimised the possibility of FIB-induced damage. A 250 nm depth increment corresponds to a FIB dose of 730 picocoulombs per micron<sup>2</sup> for MP35N and nitinol.

The micro-scale ring core proposed by Korsunsky was used in this investigation, and an image of this geometry is shown in the image of a nitinol test in Figure 17 [7]. This geometry was selected because it resolves stresses biaxially and has uniform strain relief across the gauge volume. In this investigation, the diameter of the ring core pillar was 5 microns and the trench width was 2 microns.

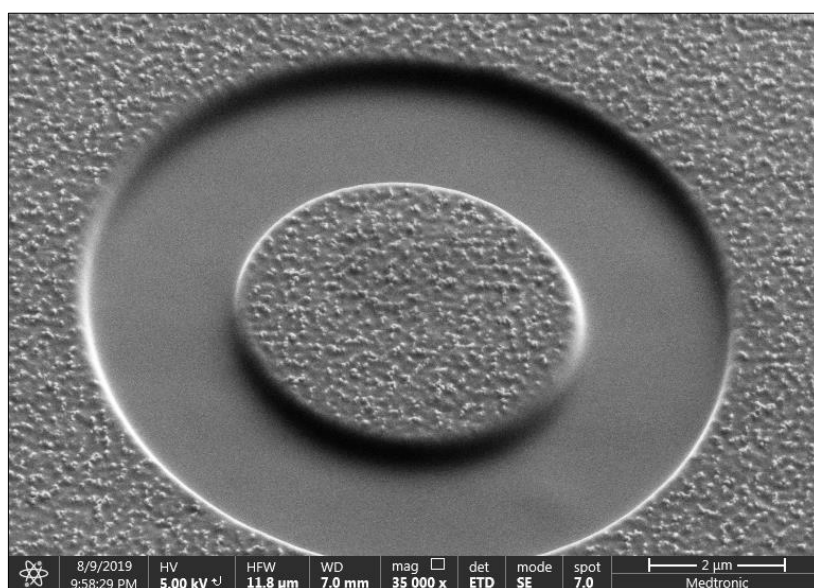


Figure 17: Image of micro-scale ring core geometry milled into nitinol test specimen near the beginning of the FIB-DIC experiment.



Developers of the ring core geometry also generated an FE computed normalised strain relief curve, in which the normalised depth, which is the milling depth divided by the pillar diameter, is plotted against the relaxation strain [7]. In this curve, most of the strain relief is released by a normalised depth of .3, with a peak at around .4. At deeper depths, strain relief saturation occurs, and the relief strain decreases, as shown in Figure 18. This curve was found to be material independent, and experimental results from previous research has matched up well with the FE computed curve.

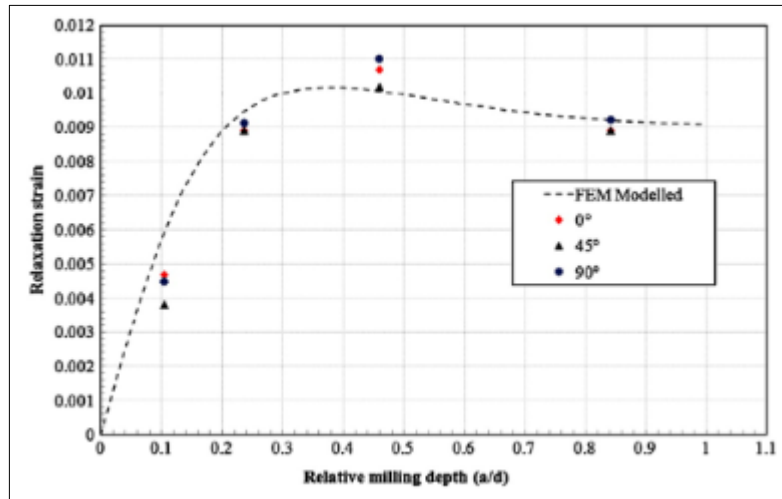


Figure 18: Typical strain relief profile for the ring core geometry [7].

## 2.4. DIC Analysis

Using Vic-2D™ software from Correlated Solutions, DIC analysis was performed on SEM images using a subset size of 31 and a step size of 7, which ensured that there would be at least 5 speckles in each subset. This gave each subset sufficient uniqueness for the DIC correlation. Incremental correlation was used, meaning that each DIC image was correlated to the previous image, rather than the reference image. This led to slightly noisier results but was necessary because the DIC software was unable to correlate images at the end of the test to the reference image because of image quality degradation over the course of the experiment.

A strain filter size of 15 was used, which, with a step size of 7, smooths the data over an area of  $15 \times 7 = 105$  pixels. The strain filter acts as a virtual strain gauge and reduces noise in the results. Engineering strain was output from the results.

The strain results in a smaller area within the gauge area, as shown by the circle in Figure 19, were then averaged and extracted. Extracting the results from a smaller area was necessary to avoid the distortions near the edge of the DIC analysis, which are present in most DIC experiments.

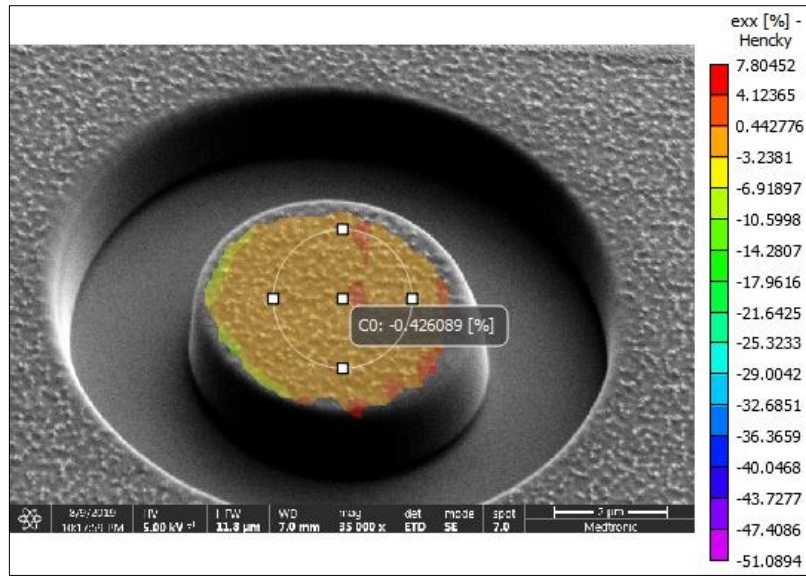


Figure 19: DIC analysis from nitinol test.

## 2.5. Calculation of Residual Stress

Once the relaxation strain was calculated through DIC, the residual stress present in the material before the milling procedure was calculated using Formula 2:

$$\sigma_x = \frac{E}{1 - \nu^2} [\Delta \epsilon_{\infty}^x + \nu \Delta \epsilon_{\infty}^y] \quad \sigma_y = \frac{E}{1 - \nu^2} [\Delta \epsilon_{\infty}^y + \nu \Delta \epsilon_{\infty}^x] \quad (2)$$

with E being the modulus of elasticity,  $\nu$  being Poisson's ratio, and  $\Delta \epsilon_{\infty}^x$  and  $\Delta \epsilon_{\infty}^y$  being the relief strain in the x and y directions achieved at the final milling depth, respectively [7].

### 3. FIB-DIC Validation

#### 3.1. Validation Method

A validation of the FIB-DIC method was performed by bending a sample and comparing the FIB-DIC results to analytical solutions. A test specimen was elastically-plastically bent in a four-point bend test. When the load was removed, residual stress was present across the profile of the bent beam. The residual stress profile was predicted using Euler beam theory and by an FE model developed by a Medtronic analyst; these solutions were compared to the FIB-DIC results.

Due to nitinol's unique superelastic properties, beam theory is unable to predict stress in a bent nitinol beam accurately enough to be used in a FIB-DIC validation [31]. Previous experiments have shown that due to nitinol's tension and compression asymmetry, the neutral axis shifts during bending. Additionally, due to strain localisation, plane sections may not remain plane during bending – a fundamental assumption of beam theory [32].

The validation was instead completed on MP35N, an alloy that is used in balloon-expandable minimally-invasive medical devices and is not superelastic. An MP35N dog bone specimen was used in this test. The dog bone is laser cut from drawn tubes, as shown in Figure 20.



Figure 20: MP35N dog bones laser cut from drawn tube.

The dog bone specimen was cut from a tube with a diameter of 6 mm and a wall thickness of .35 mm. The gauge width of the specimen was .811 mm and the length was 62.78 mm. The specimen was annealed and electropolished prior to the four-point bend test. Due to significant issues obtaining electropolished MP35N samples, the validation was completed after the FIB-DIC test on nitinol.

The dog bone was placed in four-point bend test grips on an Instron universal testing machine, as shown in Figure 21. Using equations from ASTM D6272-17, “Standard Test Method for Flexural Properties,” the centreline of the beam was deflected to a depth of 2.61 mm, which was predicted to induce plasticity across the concave and convex sections of the beam, while leaving the middle 50% of the beam elastic. After the specimen was deflected, the loading grips were then slowly raised until the load cell dropped to zero newtons – at this point, the residual displacement of the beam centreline was recorded as 1.31 mm.

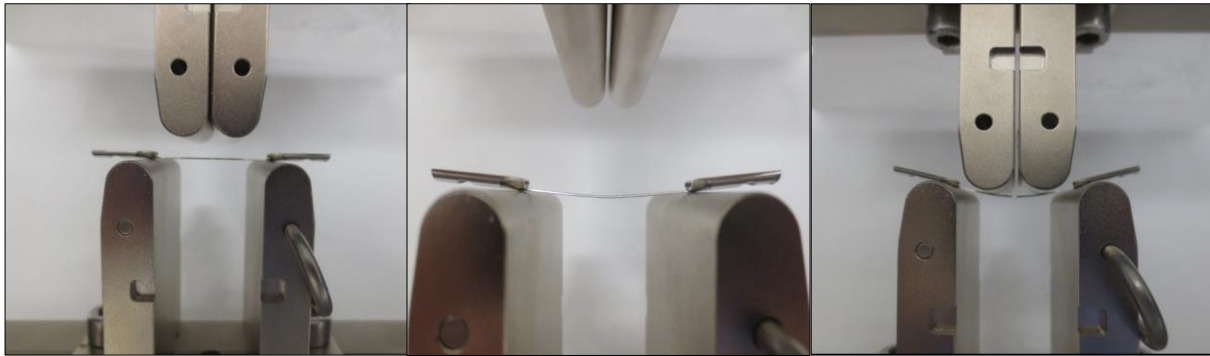


Figure 21: Left: MP35N specimen before bend test. Middle: MP35N specimen at deflection of 2.61 mm. Right: MP35N specimen after bend test with residual displacement of 1.31 mm.

The crosshead extension and load data from the four-point bend test is below in Figure 22, along with the theoretical prediction.

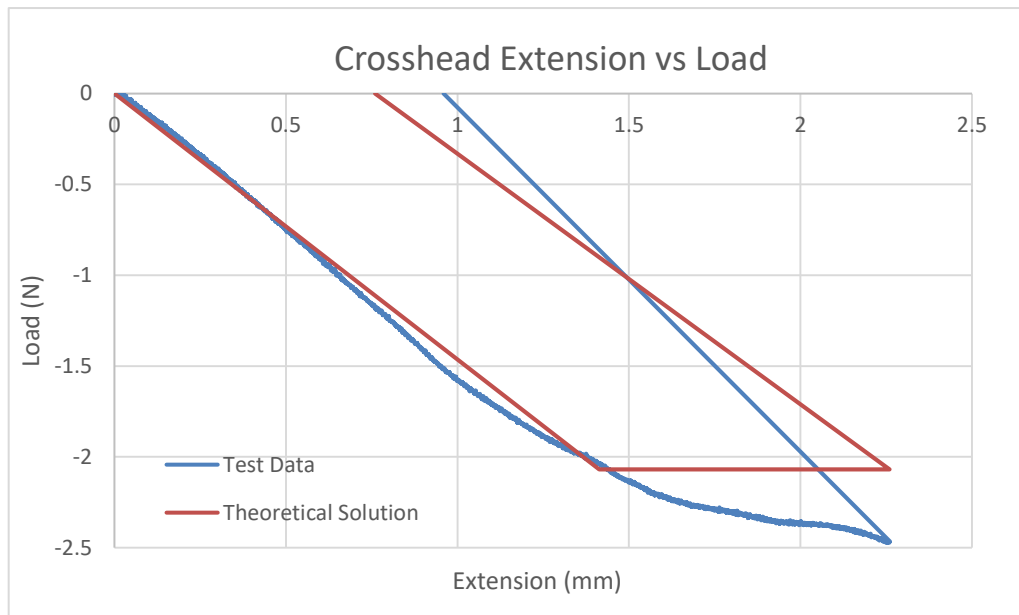


Figure 22: Four-point bend test data and theoretical prediction.

The theoretical solution matches up well with the test data, and the theory accurately predicts where the specimen will yield and comes close to predicting the residual deflection. The theory assumes elastic-perfectly plastic material behaviour, but a significant amount of work hardening occurs.

To consider work hardening and the fact that the dog bone was cut from a circular tube, a Medtronic FE analyst also simulated this four-point bend test, and a screenshot of this simulation is illustrated in Figure 23.

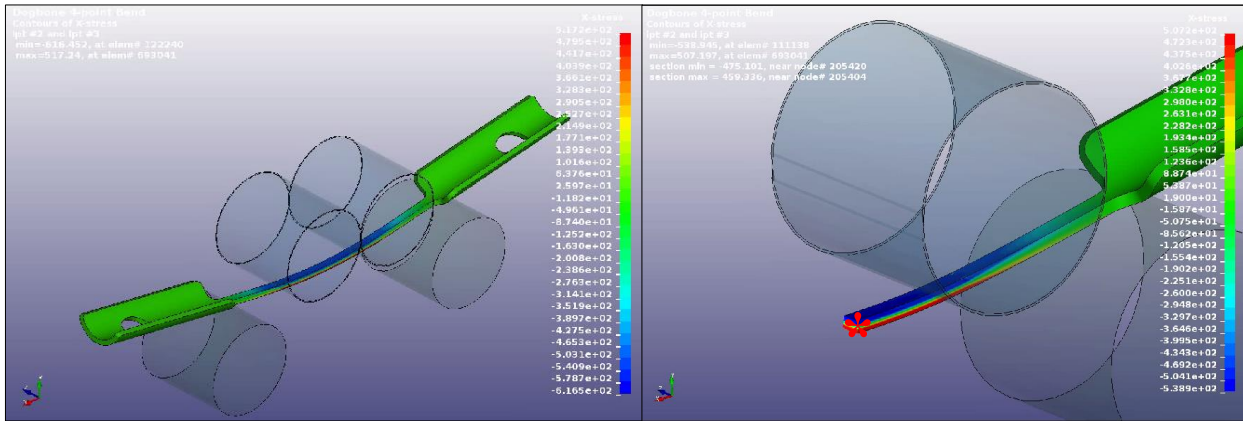


Figure 23: Left: FE simulation of four-point bend test. Right: Symmetric FE simulation of four-point bend test with \* indicating residual stress gradient across beam profile.

After completion of the bend test, the residual stress gradient across the profile of the beam was predicted using the theoretical and FE solutions.

The dog bone was then attached to an SEM pin stub, using silver paint to improve conductivity, and then speckled. Using the methods described in “Section 2: FIB-DIC Method”, micro-scale ring cores were milled into the profile of the beam in 10 250 nm depth increments to a final depth of 2.5 microns, which was deep enough to achieve strain relief saturation. Four repeat SEM images were taken after each milling step. Figure 24 shows SEM images of a ring core in MP35N at shallow and deep milling depths.

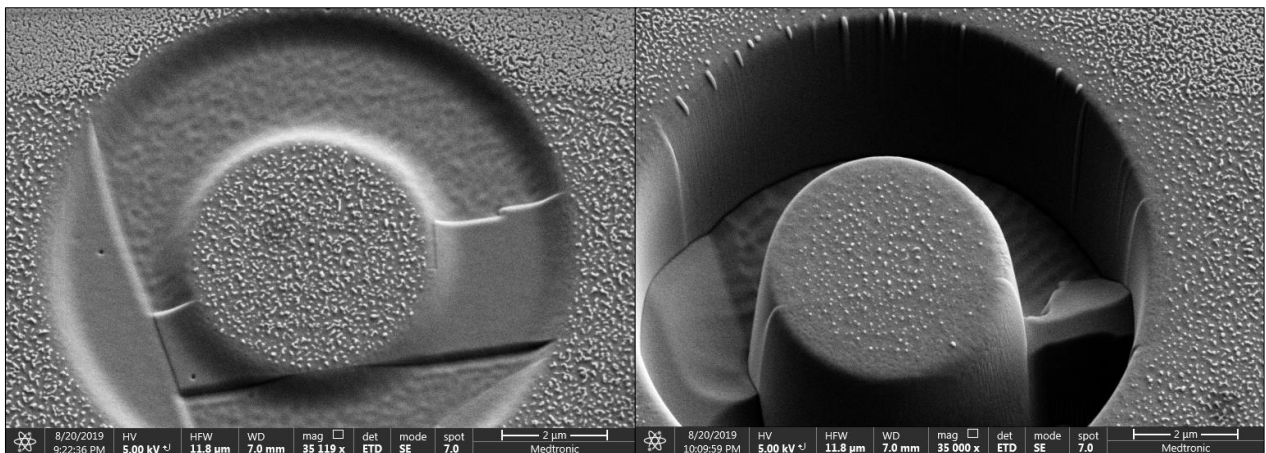


Figure 24: Ring-core geometry milled into MP35N specimen, Left: at a shallow depth, Right: at a deep milling depth.

Four micro-scale ring cores were milled in different points along the specimen profile, and the exact position of each ring core was measured after the test using an optical microscope, as shown in Figure 25. Ring cores 1 and 4 were placed in locations near the concave and convex edges of the beam, respectively, but with enough distance from the edge to avoid edge effects. Ring cores 2 and 3 were placed in locations far enough away from adjacent ring cores to avoid potential residual stress impacts from FIB milling in nearby locations.



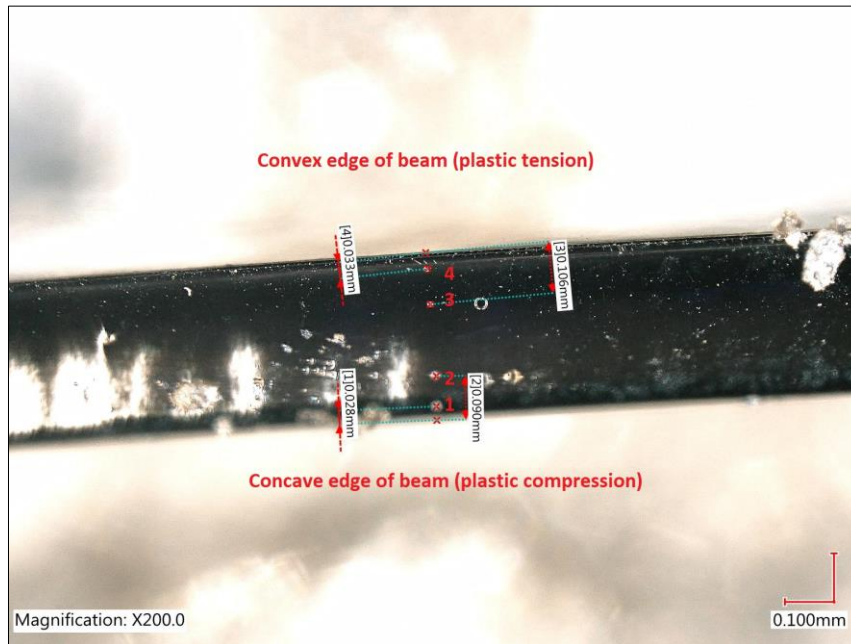


Figure 25: Optical microscope capture of 4 ring cores milled into profile of specimen.

DIC analysis was then performed on each ring core. A screenshot from a DIC analysis on a ring core in MP35N is shown in Figure 26. The residual stress at each ring core location was then calculated. Since the exact position of each ring core was known, the residual stress results from each ring core could be directly compared with the theoretical and FE solutions.

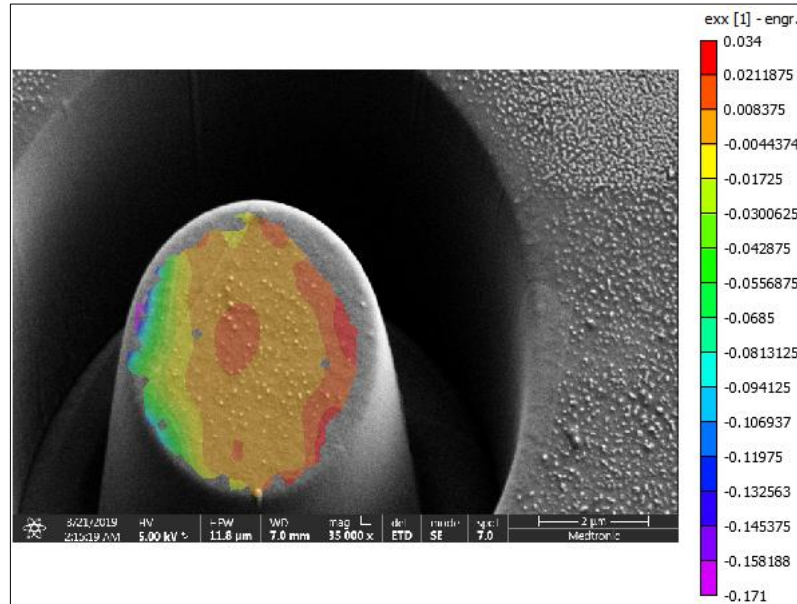


Figure 26: DIC analysis of ring core in MP35N.

## 3.2. Validation Results

### 3.2.1. Strain Relief Measurements

The strain relief in the x and y directions was measured in the DIC analysis, but only the strains in the x direction are shown below, as this is the direction affected by beam bending.

Although the strain in the y direction affects the residual stress result, these strains simply show scatter, which is expected.

The average strain in the x direction from the four repeat SEM images in Ring Core 1 is shown in Figure 27.

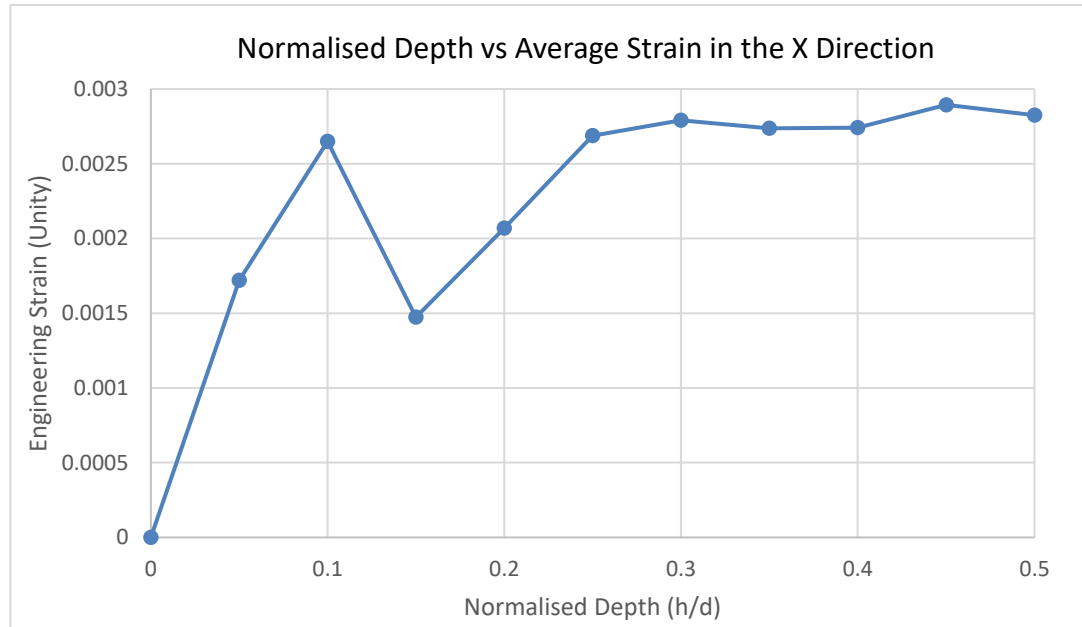


Figure 27: Relief strain in the x-axis direction for Ring Core 1.

Although the expected shape of the strain relief curve in Figure 18 is roughly followed, a smooth curve is not obtained due to the strain rapidly increasing and decreasing at the beginning of the experiment.

The strain relief in the x direction in Ring Core 2 is shown in Figure 28.

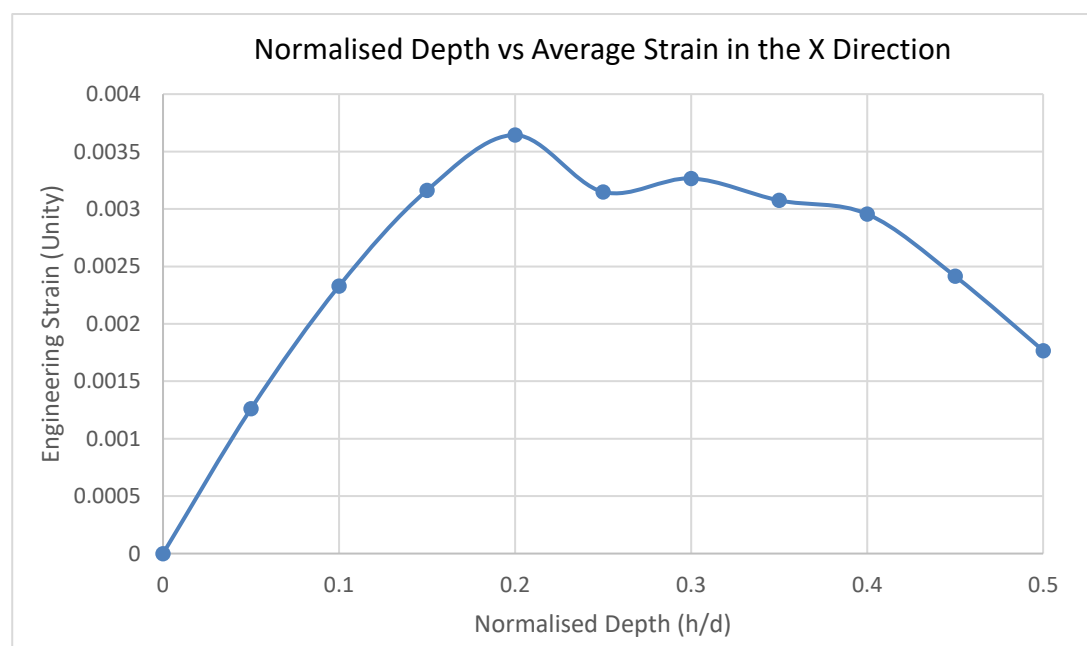


Figure 28: Relief strain in the x-axis direction for Ring Core 2.

Although strain saturation occurs, and the expected relief profile is followed in the beginning of the experiment, the strain rapidly drops off after saturation occurs, which was unexpected.

The strain relief in the x direction in Ring Core 3 is shown in Figure 29.

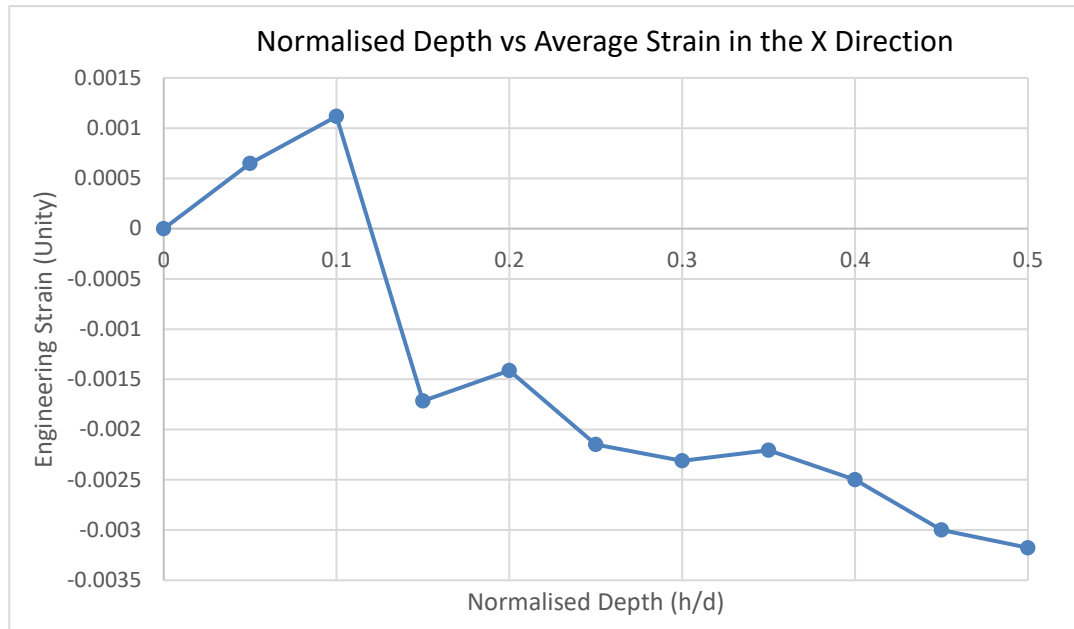


Figure 29: Relief strain in the x-axis direction for Ring Core 3.

The strain relief originally starting as positive relief is unexpected, and the results do not follow the expected smooth relaxation curve.

The strain relief in the x direction from Ring Core 4 is shown in Figure 30.

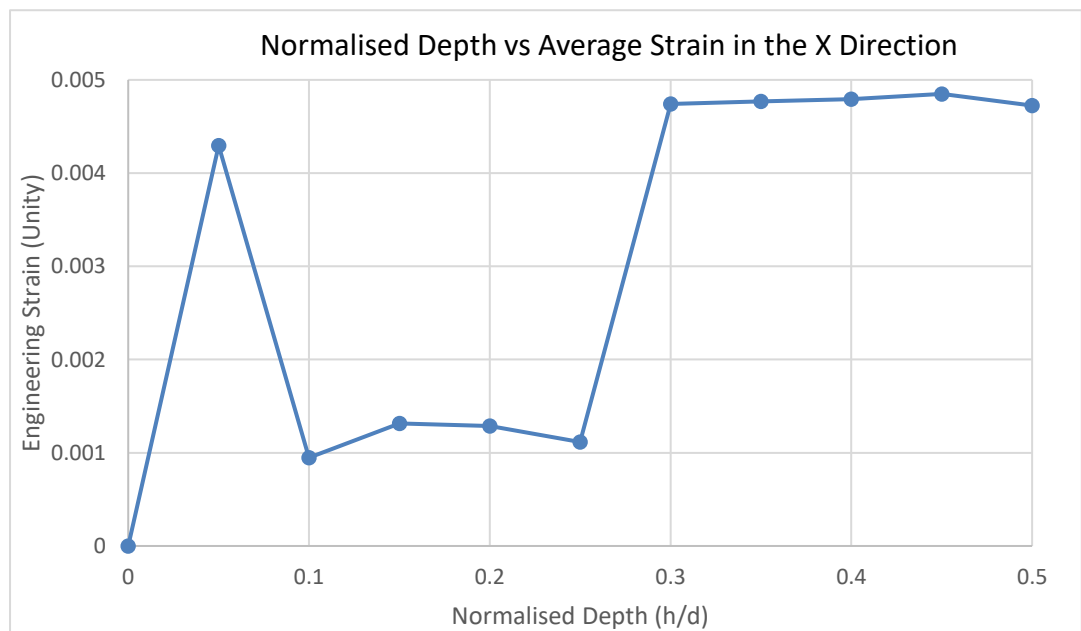


Figure 30: Relief strain in the x-axis direction for Ring Core 4.



This ring core has the highest amount of scatter, with the strain rapidly decreasing and approaching zero midway through the test.

### 3.2.2. Residual Stress Results

The residual stress measurements at the four ring core locations and the theoretical and FE solutions are shown in Figure 31. The x-axis is divided into twenty elements going from the bottom to the top of the beam. Ring Cores 1 through 4 were also milled from the bottom to the top of the beam.

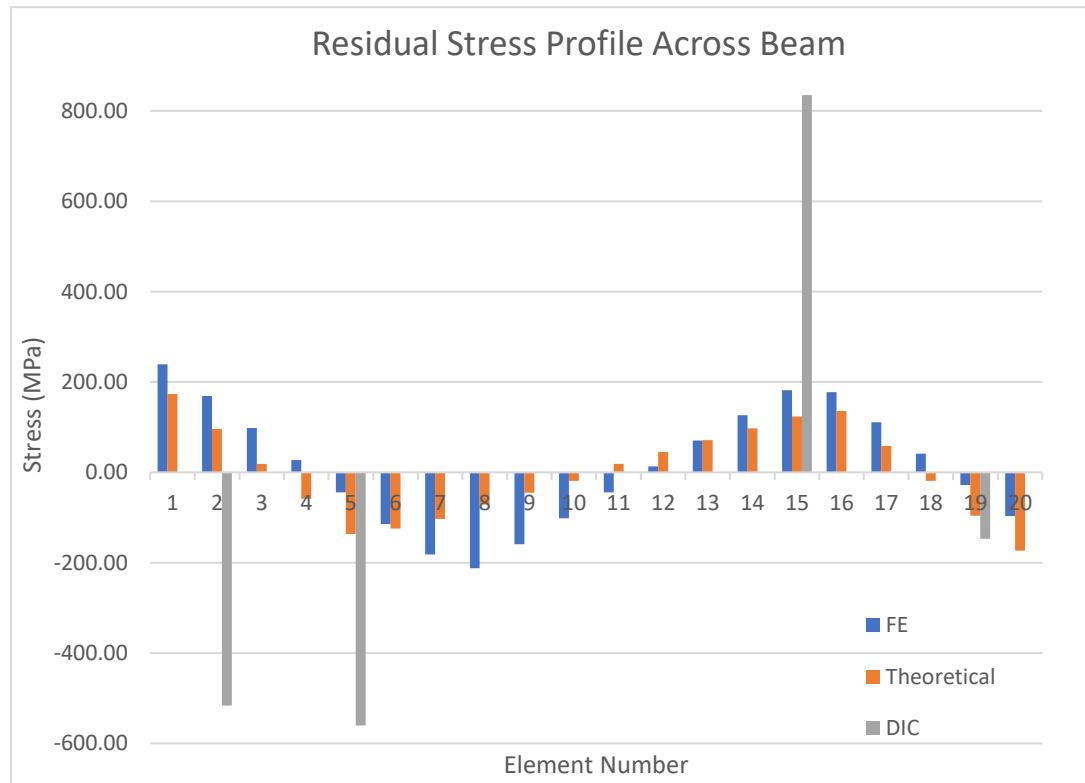


Figure 31: Residual stress measurements from FIB-DIC and theoretical and FE predictions.

The FIB-DIC results do not track well with the theoretical and FE solutions, although the overall residual stress trend is roughly followed. The stress measurements from FIB-DIC are higher than the stresses predicted by the theoretical and FE solutions, which are in close agreement. Except for Ring Core 1, which was milled near the bottom of the beam at Element 2, the FIB-DIC results match the overall residual stress trend expected for a beam after bending. The deviation from the analytical solutions is most likely due to the field emission gun (FEG), which is the electron beam source, nearing the end of its lifecycle. The decreased quality of the FEG caused images to become blurry throughout the FIB-DIC experiment and constant re-focusing was required.

## 4. Nitinol Test

### 4.1. Test Method

A FIB-DIC test measured the residual stress in a nitinol wire. The nitinol wire had a diameter of .4064 mm and was annealed and electropolished prior to testing.

The nitinol wire was crimped multiple times, simulating the deformations the material would experience before being loaded into a catheter; this process induced plasticity and is shown by the FE model of the crimping process in Figure 32.

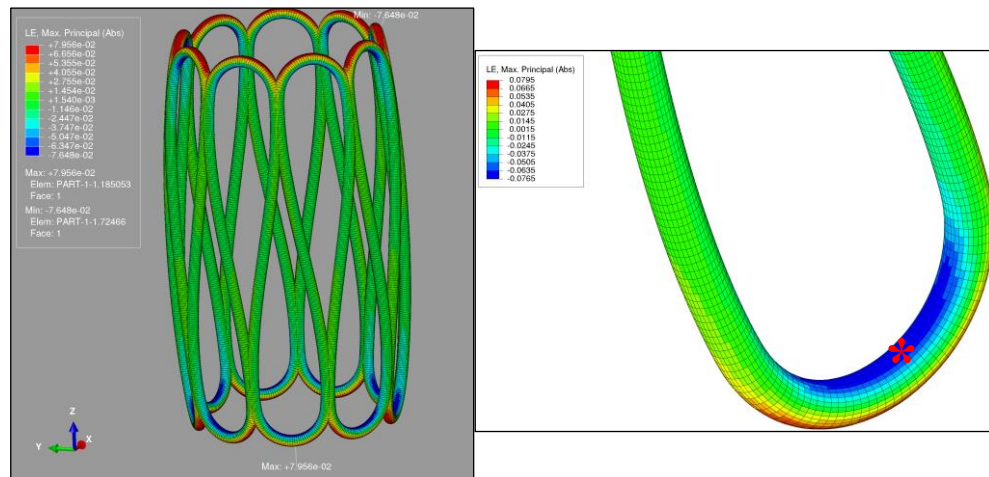


Figure 32: Left: FE model of crimped nitinol wire. Right: Zoomed-in view of concave section of wire with \* indicating ring core location.

This wire was manufactured with an Austenite Finish ( $A_f$ ) temperature of  $10 \pm 5$  °C. The FIB-DIC test was performed at room temperature, which was above the  $A_f$  temperature. This allowed the superelastic properties of nitinol to be probed. After crimping, the wire was cut so that it could fit in the SEM. It was then attached to an SEM pin stub using silver paint and speckled.

1 ring core was milled into the middle of the concave section of the wire, as shown in Figure 32, which experienced plastic compressive stress during crimping and would have had tensile residual stress induced after the crimping force was removed. 17 250 nm milling increments were used to mill to a final depth of 4.25 microns. Although the strain was fully relieved before this depth, 4.25 microns was chosen to allow the relaxation curve of nitinol to be more fully characterised. 3 repeat SEM images were taken at each milling step. Images of the fully milled ring core on the nitinol sample are shown in Figure 33.

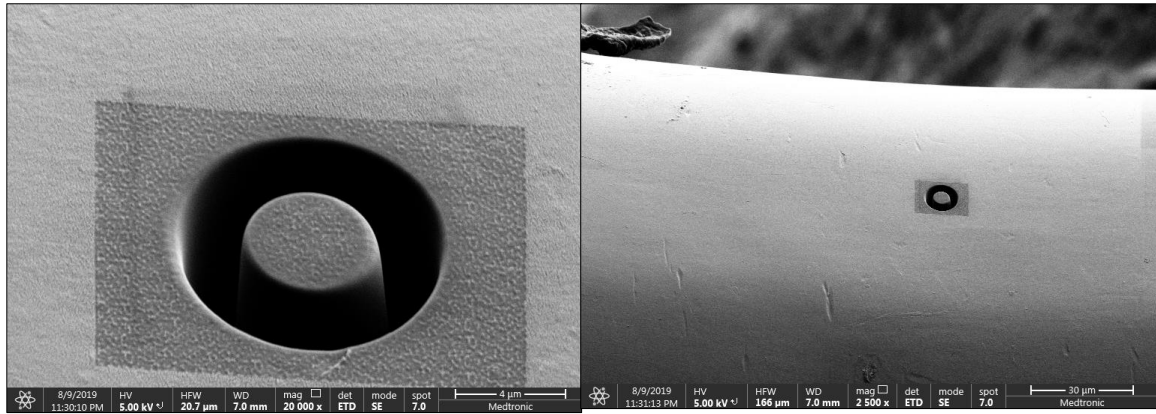


Figure 33: Left: Fully milled ring core in nitinol sample. Right: Zoomed-out view of ring core on concave edge of nitinol sample.

#### 4.2. Test Results

The relief strain in the x direction, which was the primary loading direction during crimping, is shown in Figure 34.

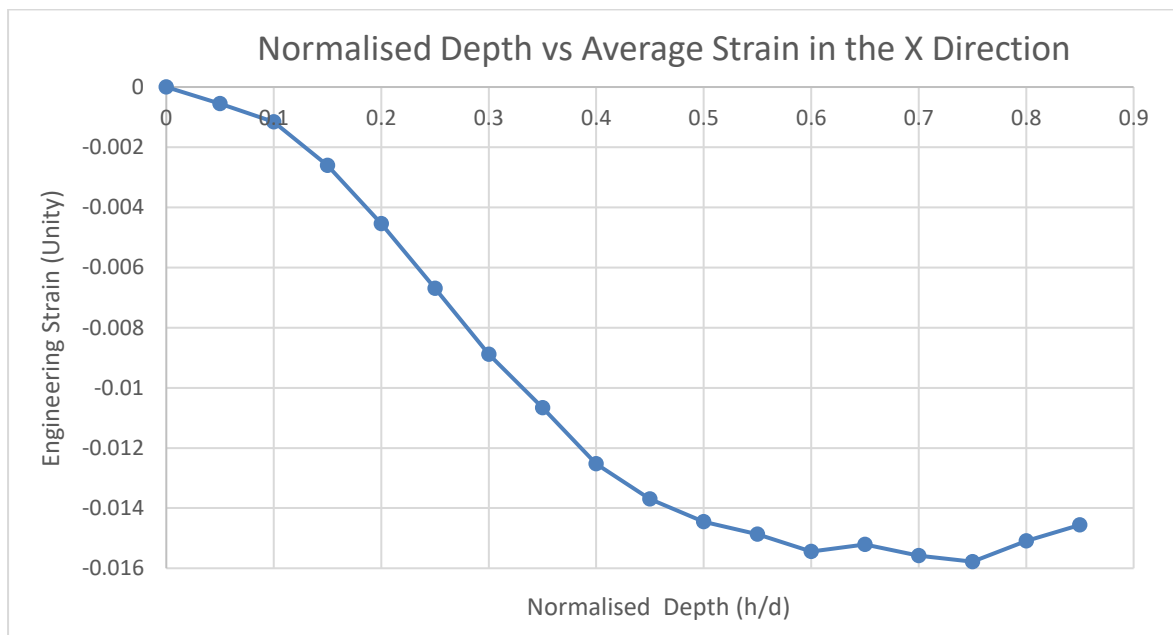


Figure 34: Relief strain in the x-axis direction for the ring core milled in nitinol.

This relaxation curve tracks well with the expected relaxation curve for the ring geometry, and strain saturation occurs at a normalised depth of .6.

The calculated residual stress was 1044 Megapascals in the x-axis direction, which was in the direction of loading, and 170 Megapascals in the y-axis direction. The FE model of the crimping process did not predict residual stress, so the FIB-DIC results were not able to be directly compared to an FE solution; however, the residual stress measurement in the x direction is in close agreement to the martensitic yield stress of nitinol tubing, which ranges from 1000-1200 Megapascals [33]. As this FIB-DIC measurement was captured in an area of the material that underwent plastic deformation, a residual stress measurement similar in value to the yield stress was expected.

## 5. Discussion & Conclusion

### 5.1. FIB-DIC Validation

Although the overall residual stress trend across the profile of the nitinol beam was roughly followed, the FIB-DIC results differed significantly from the analytical solutions. This is most likely due to the FEG nearing the end of its lifecycle. Other users of the FEI noticed focusing issues at magnifications as low as 10,000, and this validation was conducted at a magnification of 35,000.

The reduced performance of the FEG made images go out of focus after almost every milling increment, so constant SEM refocusing was required. As seen in Figure 24, refocusing caused the magnification to change slightly during the test, which probably had a significant effect on the DIC analysis. The large jumps in the MP35N strain relief profiles, which do not follow a smooth relief curve, are also most likely due to refocussing between milling increments.

Additionally, uniform milling was not achieved in the ring cores. MP35N has a grain size of around 12 microns, so a 5 micron ring core could have been milled between two grains, which is what occurs in Figure 24. Nonuniform milling may have had an impact on the relaxation strains as well.

Finally, the analytical solutions have weaknesses. MP35N is technically orthotropic, since it is cut from a tube that was drawn, but the material was considered as isotropic in the theoretical and FE solutions. Also, even after annealing and electropolishing, the test specimen was most likely not completely stress-free before the four-point bend test, so the FIB-DIC results may be measuring residual stress induced during manufacturing. The analytical solutions do not account for this. Ideally, this validation would have been performed on a completely stress-free nitinol beam with uniform FIB milling using a quality FEG.

### 5.2. Nitinol Test

For the first time, residual stress in superelastic nitinol was successfully measured using FIB-DIC. Since the nitinol test was performed several weeks before the FIB-DIC validation, the FEG functioned as intended. There was no need to re-focus throughout the test, and a smooth strain relief profile was output.

The nitinol relaxation curve tracks well with the expected relaxation curve for the ring core geometry. Strain saturation occurs at a normalised depth of .6, which is deeper than the typical strain relief saturation depth of .4, as seen in Figure 18. Past studies have indicated that the normalised strain relief profile is material independent, but these studies have not probed residual stress in a superelastic material, such as nitinol. Future experiments should confirm that the nitinol strain relief curve slightly differs from the typical strain relief curve. The residual stress measurement was in close agreement with the yield stress of nitinol, which was expected.

FIB-DIC has been shown to be an effective method to measure residual stress in nitinol and has a high potential for use in building understanding of nitinol's complex properties. A potential future use of the technique is improving the accuracy of state-of-the-art superelastic material models for the medical device industry, which can lead to design changes for improved device performance.

The use of minimally-invasive medical devices is growing rapidly, and as regulatory bodies begin to expand indications for these devices – allowing younger, healthier patients to consider less

invasive medical procedures – the growth of these devices will increase even further. As the adoption of these devices grows, so will expectations about their quality and longevity. FIB-DIC may be used as a powerful technique to improve the performance and structural integrity of these devices, which can ultimately lead to improved clinical outcomes for patients.

## 6. References

1. Ralph Ivan Stephens & Al, E 2001, *Metal fatigue in engineering*, 2nd edition, Wiley, Cop, New York, pp. 245–246.
2. Dieter, G 1988, *Mechanical Metallurgy*, SI Metric Edition, Mcgraw-Hill, Singapore, pp. 409–410.
3. Withers, PJ & Bhadeshia, HKDH 2001, “Residual stress. Part 1 – Measurement techniques”, *Materials Science and Technology*, vol. 17, no. 4, pp. 355–365.
4. *Measurement of Residual Stresses by the Hole-Drilling Strain Gage Method* 2010, *vishaypg.com*, 1 November, Vishay Precision Group, viewed 30 May 2019, <<http://www.vishaypg.com/docs/11053/tn503.pdf>>.
5. Prev y, P n.d., *X-RAY DIFFRACTION RESIDUAL STRESS TECHNIQUES*, *lamdatechs.com*, Lamda Technology, viewed 30 May 2019, <<https://www.lamdatechs.com/wp-content/uploads/200.pdf>>.
6. Lord, J, Cox, D & Ratzke, A 2018, *A good practice guide for measuring residual stresses using FIB-DIC*, *Good Practice Guide 143*, National Physical Laboratory, pp. 1–172, viewed 5 January 2019, <<http://eprintspublications.npl.co.uk/7807/>>.
7. Korsunsky, A.M., Sebastiani, M. & Bemporad, E. 2009, "Focused ion beam ring drilling for residual stress evaluation", *Materials Letters*, vol. 63, no. 22, pp. 1961-1963.
8. Ritter, M. and Hemmleib, M. 2006. “SEM/FIB stage calibration with photogrammetric methods”, In: *ISPRS Commission V Symposium*.
9. LePage, W 2009, *A Practical Guide to DIC*, *Digitalimagecorrelation.org*, viewed 28 May 2019, <<https://digitalimagecorrelation.org/>>.
10. Speckle Generator. (2014). Correlated Solutions, Inc.
11. Sutton, M, Wolters, W, Peters, W, Ranson, W & McNeill, S 1983, “Determination of displacements using an improved digital correlation method”, *Image and Vision Computing*, vol. 1, no. 3, pp. 133–139.
12. Benoit, A., Gu rard, S., Gillet, B., Guillot, G., Hild, F., Mitton, D., P ri , J. & Roux, S. 2009, "3D analysis from micro-MRI during in situ compression on cancellous bone", *Journal of Biomechanics*, vol. 42, no. 14, pp. 2381-2386.
13. Roux, S., Hild, F., Viot, P. & Bernard, D. 2007, "Three dimensional image correlation from X-Ray computed tomography of solid foam", *Composites Part A: Applied Science and Manufacturing*, vol. 39, no. 8, pp. 1253-1265.
14. Kang, K.J., Yao, N., He, M.Y. & Evans, A.G. 2003, "A method for in situ measurement of the residual stress in thin films by using the focused ion beam", *Thin Solid Films*, vol. 443, no. 1, pp. 71-77.
15. Sabat , N., Vogel, D., Gollhardt, A., Keller, J., Can , C., Gr cia, I., Morante, J.R. & Michel, B. 2006, "Measurement of residual stress by slot milling with focused ion-beam equipment", *Journal of Micromechanics and Microengineering*, vol. 16, no. 2, pp. 254-259.
16. Krottenthaler, M., Benker, L., Mughal, M.Z., Sebastiani, M., Durst, K. & G ken, M. 2016, "Effect of elastic anisotropy on strain relief and residual stress determination in cubic systems by FIB-DIC experiments", *Materials & Design*, vol. 112, pp. 505-511.

17. Salvati, E. & Korsunsky, A.M. 2017, "An analysis of macro- and micro-scale residual stresses of Type I, II and III using FIB-DIC micro-ring-core milling and crystal plasticity FE modelling", *International Journal of Plasticity*, vol. 98, pp. 123-138.
18. Everaerts, J., Salvati, E., Uzun, F., Romano Brandt, L., Zhang, H. & Korsunsky, A.M. 2018, "Separating macro- (Type I) and micro- (Type II+III) residual stresses by ring-core FIB-DIC milling and eigenstrain modelling of a plastically bent titanium alloy bar", *Acta Materialia*, vol. 156, pp. 43-51.
19. Korsunsky, A.M., Sebastiani, M. & Bemporad, E. 2010, "Residual stress evaluation at the micrometer scale: Analysis of thin coatings by FIB milling and digital image correlation", *Surface & Coatings Technology*, vol. 205, no. 7, pp. 2393-2403.
20. Sebastiani, M 2019, *iSTRESS Project*, Roma Tre University, viewed 30 January 2019, <<http://uniroma3-web.sharepoint.com/ricerca/stm/istress>>.
21. Salvati, E, Benedetti, M, Sui, T & Korsunsky, AM 2016, "Residual Stress Measurement on Shot Peened Samples Using FIB-DIC", *Residual Stress, Thermomechanics & Infrared Imaging, Hybrid Techniques and Inverse Problems, Volume 9*, vol. 9, pp. 275–283.
22. Zhu, R., Xie, H., Dai, X., Zhu, J. & Jin, A. 2014, "Residual stress measurement in thin films using a slitting method with geometric phase analysis under a dual beam (FIB/SEM) system", *Measurement Science and Technology*, vol. 25, no. 9, pp. 95003.
23. O'Connor, S.J., Nowell, D. & Dragnevski, K.I. 2016, "Measurement of fatigue crack deformation on the macro- and micro-scale: Uniform and non-uniform loading", *International Journal of Fatigue*, vol. 89, pp. 66-76.
24. Nowell, D., Dragnevski, K.I. & O'Connor, S.J. 2018, "Investigation of fatigue crack models by micro-scale measurement of crack tip deformation", *International Journal of Fatigue*, vol. 115, pp. 20-26.
25. Nowell, S.C. & Nowell, D. 2019, "A comparison of recent models for fatigue crack tip deformation", *Theoretical and Applied Fracture Mechanics*, vol. 103, pp. 102299.
26. Salvati, E., O'Connor, S., Sui, T., Nowell, D. & Korsunsky, A.M. 2016, "A study of overload effect on fatigue crack propagation using EBSD, FIB–DIC and FEM methods", *Engineering Fracture Mechanics*, vol. 167, pp. 210-223.
27. Fleury, R.M.N., Salvati, E., Nowell, D., Korsunsky, A.M., Silva, F. & Tai, Y.H. 2019, "The effect of surface damage and residual stresses on the fatigue life of nickel superalloys at high temperature", *International Journal of Fatigue*, vol. 119, pp. 34-42.
28. Medtronic.com. 2019. *TAVR Heart Valve Replacement Procedure*. [online] Available at: <https://www.medtronic.com/us-en/patients/treatments-therapies/transcatheter-aortic-valve-replacement/about/tavr-procedure.html> [Accessed 2 Sep. 2019].
29. Everaerts, J., Song, X., Nagarajan, B. & Korsunsky, A.M. 2018, "Evaluation of macro- and microscopic residual stresses in laser shock-peened titanium alloy by FIB-DIC ring-core milling with different core diameters", *Surface & Coatings Technology*, vol. 349, pp. 719-724.
30. Mansilla, C., Ocelik, V. & De Hosson, Jeff T. M 2014, "A New Methodology to Analyze Instabilities in SEM Imaging", *Microscopy and Microanalysis*, vol. 20, no. 6, pp. 1625-1637.
31. Wick, A, Vöhringer, O & Pelton, AR 1995, "The Bending Behavior of NiTi", *Journal de Physique IV*, vol. 05, no. C8, pp. C8-789-C8-794.

32. Reedlunn, B., Churchill, C.B., Nelson, E.E., Shaw, J.A. & Daly, S.H. 2014, "Tension, compression, and bending of superelastic shape memory alloy tubes", *Journal of the Mechanics and Physics of Solids*, vol. 63, pp. 506-537.
33. Xiao-Yan, G., Alan, P. and Tom, D. 2003. "Finite Element Analysis and Experimental Evaluation of Superelastic Nitinol Stent", In: *Shape Memory and Superelastic Technologies*. TIPS Technical Publishing, pp.453-462.